PROCEEDINGS OF SCIENCE

Radio continuum emission predominantly traces star-formation in radio-quiet active galactic nuclei

GT. Kekana,[a,*] **S. Kolwa,**[b] **K. Thorat**[c] **and S. Razzaque**[a,d,e]

[a] *Centre for Astro-Particle Physics (CAPP) and Department of Physics, University of Johannesburg, PO Box 524, Auckland Park 2006, South Africa*

[b] *Department of Mathematical Sciences, University of South Africa, Cnr Christian de Wet Rd and Pioneer Avenue, Florida Park, 1709 Roodepoort, South Africa*

[c] *Department of Physics, University of Pretoria, Hatfield, Pretoria 0028, South Africa*

[d] *Department of Physics, The George Washington University, Washington, DC 20052, USA*

[e] *National Institute for Theoretical and Computational Sciences (NITheCS), Private Bag X1, Matieland, South Africa*

E-mail: gthandokekana@gmail.com, kolwasn@unisa.ac.za, kshitijthorat.astro@gmail.com, srazzaque@uj.ac.za

We investigate whether radio emission primarily traces star formation in radio-quiet active galactic nuclei (RQ AGN). Our sample consists of 5223 galaxies detected by the MeerKAT International GHz Tiered Extragalactic Exploration (MIGHTEE) survey with multi-wavelength counterparts up to a z $\approx$ 6 limit. The sources were classified using the infrared-to-radio luminosity ratio (q_{IR}), X-ray luminosity cuts, and mid-infrared colour cuts into RQ AGN (8.9%), radio-loud AGN (RL AGN, 33.2%), and star-forming galaxies (SFGs, 55.4%). We calibrated the star formation rate (SFR)-1.4 GHz radio luminosity ($L_{1.4\ \mathrm{GHz}}$) relation for both SFGs and RQ AGN. We found that SFRs correlate positively with $L_{1.4\ \mathrm{GHz}}$ for both populations, which was expected since they are both non-radio excess and they follow the infrared-radio correlation. From the SFR-$L_{1.4\ \mathrm{GHz}}$ correlation, we measured the average Spearman's rank correlation coefficients (ρ) of $\rho_{\mathrm{SFGs}} \approx 0.806 \pm 0.004$ and $\rho_{\mathrm{RQ\ AGN}} \approx 0.805 \pm 0.009$, and best-fit slopes ($m$) of $m_{\mathrm{SFGs}} \approx 0.866 \pm 0.006$ and $m_{\mathrm{RQ\ AGN}} \approx 0.926 \pm 0.003$, respectively. The similarity between the measured slopes and Spearman's coefficients for both SFGs and RQ AGN indicates that radio continuum emission in RQ AGN mainly traces star formation.

High Energy Astrophysics in Southern Africa (HEASA2025)
16-20 September, 2025
University of Johannesburg, South Africa

*Speaker

 ISSN 1824-8039 . Published by SISSA Medialab.

PoS(HEASA2025)028

1. Introduction

Radio continuum emission is a key tracer for star formation (SF) and is mainly dominated by non-thermal emission produced when relativistic electrons spiral within the magnetic fields [24, 25]. Radio emission is dust-unbiased because of its longer wavelengths ($\lambda \cong 0.3\ mm - 15\ m$ [36]), allowing for the detection of dust-obscured sources such as the star-forming galaxies (SFGs) and radio-quiet active galactic nuclei (RQ AGN). RQ AGN are identified as non-radio excess sources with a radiative-mode AGN [5]. They are classified as non-radio excess sources using the logarithmic infrared-to-radio ratio (quantified as q_{IR}) or using a radio luminosity to star formation rate (SFR) relation [1, 26–28]. The raditive-mode AGN can be identified using multi-wavelength diagnostics, such as X-ray luminosity cuts [3] and mid-infrared (MIR) colour cuts [4].

The physical origin of radio emission in RQ AGN is still actively debated in radio astronomy. This is because radio emission in RQ AGN can trace several emission mechanisms, such as SF, low-power jets, coronal disc emission, AGN-driven winds, or thermal emission, which usually comes from the heated dust or ionized gas [2]. Some studies found radio emission in RQ AGN to be primarily tracing SF [e.g., 32], in [29–31] they found radio emission to be mainly tracing AGN activity, meanwhile in [33] they found radio emission to be possibly tracing winds, radio jets, or compact starbursts. This uncertainty in disentangling radio driven emission mechanisms in RQ AGN, shows the need for deep radio surveys such as the MeerKAT International GigaHertz Tiered Extragalactic Exploration (MIGHTEE; [34]) survey and the upcoming telescopes, such as the Square Kilometer Array (SKA; [35]), which will clearly separate AGN activity and SF because of its sensitivity and resolution. Therefore, this work aims to fill in the gap by calibrating the SFR-1.4 GHz radio luminosity ($L_{1.4\ \mathrm{GHz}}$) relation for RQ AGN detected with the MIGHTEE survey.

2. Data Sample

In this study, we use data from the MeerKAT radio telescope, a precursor to the Square Kilometre Array (SKA) mid-frequency telescope [9]. MeerKAT has undertaken several large survey projects (LSPs), one of which is the MIGHTEE survey. MIGHTEE is a deep radio survey that aims to study galaxy evolution through three observations: continuum, spectral line, and polarization. When complete, MIGHTEE will cover 20 deg^2 across four different fields; namely, the COSMOS, the XMM-Newton Large Scale Structure (XMM-LSS), the European Large Area Infrared Survey South 1 (ELAIS-S1), and the Extended Chandra Deep Field-South (E-CDFS). For this study, we use the MIGHTEE Early Science images from the COSMOS field, which were optimised for higher sensitivity (Briggs robustness parameter [10] of 0.0) while mitigating confusion. The resulting images reach an rms thermal noise of 1.7 μJy beam^{-1} with a circular synthesized beam of full width at half-maximum (FWHM) diameter of 8.6 arcsec. These images were observed in L-band (centred at 1.28 GHz) for 17.45 hours on-source time focusing on a single pointing at RA 10h:00m:28.6s and Dec +02d:12m:21s. Source extraction was carried out using the PYTHON Blob Detector and Source Finder (PyBDSF; [11]), and the extracted catalogue contains 5223 radio sources above a 5σ detection limit, with flux densities ranging from 8 μJy to 90 mJy and spanning redshifts up to $z \approx 6$.

Module	Parameter	Values
Star formation history SFR $\propto$ t exp (-t/τ)	Stellar e-folding time	100,500,1000,5000 Myr
	Stellar age	500,1000,3000,5000,7000 Myr
Stellar population [38]	Initial mass function	[37]
Dust attenuation [39]	Color excess of the nebular lines	0.05, 0.1, 0.2, 0.3, 0.4, 0.5, 0.7, 0.9
Dust emission [40]	Slope in $\mathrm{d}M_{\mathrm{dust}} \propto U^{-\alpha} dU$	2.0,2.5
AGN SKIRTOR	AGN contribution to IR luminosity	0.01, 0.1, 0.2, 0.3, 0.4, 0.5, 0.6, 0.7, 0.8, 0.99
	Viewing angle	30,60,90
	Polar-dust color excess	0, 0.01, 0.02, 0.05, 0.1, 0.15, 0.2, 0.3, 0.4, 0.5, 0.6
Radio	Far IR-to-radio correlation coefficient for SF	2.4, 2.5, 2.6, 2.7
	AGN optical radio-loudness	0.01, 0.02, 0.05, 0.1, 0.2, 0.5,10, 1000, 2000, 5000, 10000

Table 1: Model parameters for CIGALE SED fitting. **Note**: For parameters not included in this table we used default values.

This catalogue was compiled by [6], consisting of the MIGHTEE COSMOS data and their multi-wavelength counterparts. The optical and near-infrared (NIR) observations were taken in *grizy*, 8160 Å and 9210 Å filters from Hyper Suprime Cam (HSC; [12]), u^*griz bands from the Canada-France-Hawaii Telescope Legacy Survey (CFHTLS; [13]), the z-band filter from *Subaru*/Suprime Cam [14], and $YJHK_{\mathrm{s}}$ bands from the *UltraVISTA* survey. The mid-infrared (MIR) and far-infrared (FIR) observations were obtained at 3.6 and 4.5 μm from the *Spitzer* Infrared Array Camera (IRAC), 5.8 and 8.0 μm bands from the *Spitzer* Large Area Survey with the HSC (SPLASH; [18]), 24 μm band from the Multiband Imaging Photometry (MIPS; [16]), 100 and 160 μm bands from the Photodetector Array Camera and Spectrometer (PACS; [15]), 250, 350, and 500 μm bands from the Spectral and Photometric Imaging receiver (SPIRE; [17]).

3. SED fitting method

We constrained the physical properties (SFRs, $M_\star$) of the radio sources in our catalogue using the Code Investigating GALaxy Emission (CIGALE[1] [19–21]) spectral energy distribution (SED) fitting code. Table 1 summarises the modules and parameters used in CIGALE to constrain the physical properties. Figure 1 shows an example SED for one source, obtained from CIGALE. To confirm the robustness of our CIGALE-derived results, we compared them to those derived in [22] using `AGNfitter` [23], and we found consistency between the two codes.

4. Radio source classification

The MIGHTEE Early Science catalogue was classified into RQ AGN, RL AGN, and SFGs using the following classification diagnostics:

- **Radio excess**: A source is classified as a radio excess source if its infrared-radio luminosity ratio (quantified as q_{IR}) value lies 0.43 dex below the best-fit q_{IR}-z-$M_\star$ correlation from [1] (i.e, equation 5 in their paper). We calculated q_{IR} using

$$q_{\mathrm{IR}} = \log\left(\frac{L_{\mathrm{IR}}[\mathrm{W}]}{3.75\times10^{12}\ \mathrm{Hz}}\right) - \log(L_{1.4\ \mathrm{GHz}}[\mathrm{W\ Hz^{-1}}]), \quad (1)$$

[1] https://cigale.lam.fr/

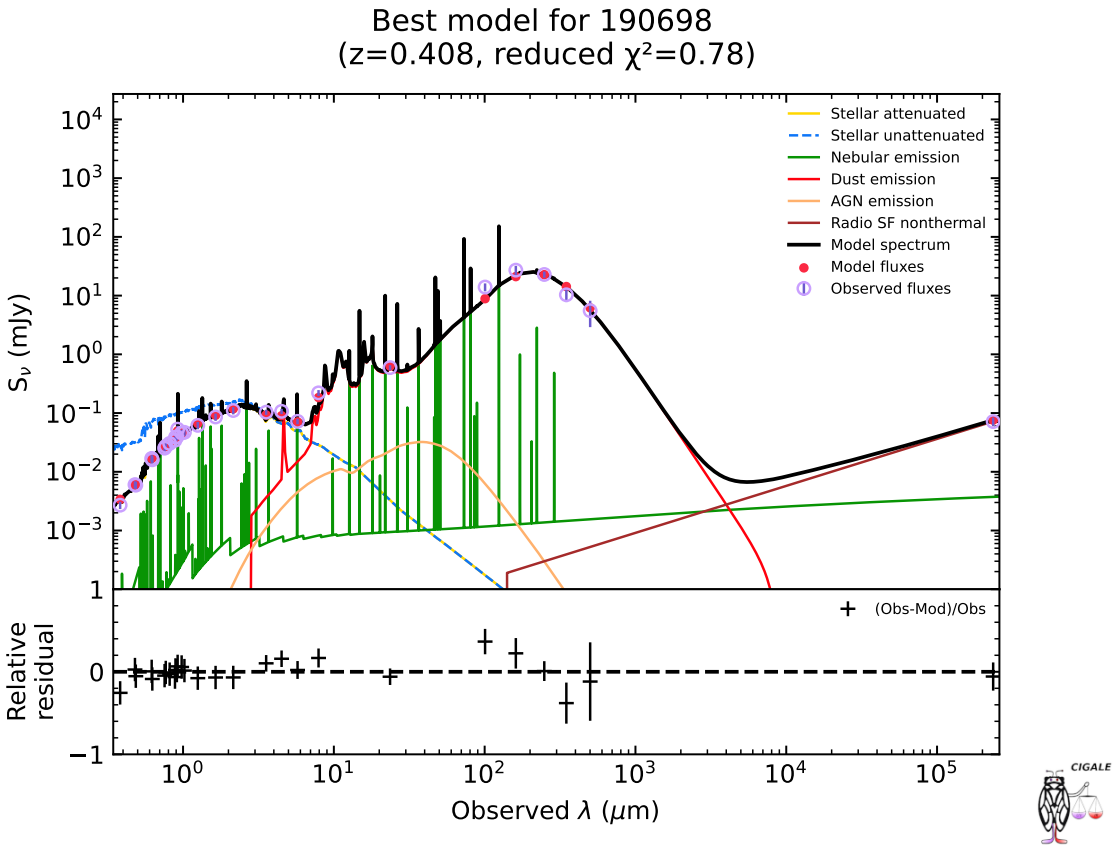

Figure 1: SED fit using CIGALE for an example MIGHTEE Early Science source flux densities. The upper panel shows the SED with different emission lines; each line and point is labeled in the legend with a similar colour coding. We have the residual between the observed and model photometry in the lower panel.

where L_{IR} is the total infrared luminosity integrated over 8 - 1000 μm, obtained from CIGALE. $L_{1.4\ \mathrm{GHz}}$ represents the rest-frame radio luminosities derived by converting the 1.28 GHz flux densities while assuming a radio spectral index of α = -0.7 (where S $\propto \nu^{\alpha}$), through

$$L_{\mathrm{rest}}[W\ Hz^{-1}] = 4\pi S_{\nu_{\mathrm{obs}}} \left(\frac{\nu_{\mathrm{rest}}}{\nu_{\mathrm{obs}}}\right)^{\alpha} \frac{D_L^2}{(1+z)^{1+\alpha}}, \tag{2}$$

where $S_{\nu_{\mathrm{obs}}}$ is the observed flux density at effective frequency ν_{obs}, ν_{rest} is the rest-frame frequency 1.4 GHz, and D_L is the luminosity distance.

- **X-ray luminosity cut**: a source is identified as X-ray AGN if $L_{\mathrm{X-ray}} > 10^{42}$ erg s^{-1} [3].
- **MIR colour cut**: a source is identified as MIR AGN if it lies within the [4] region in a $S_{8.0\ \mu\mathrm{m}}/S_{4.5\ \mu\mathrm{m}}$ vs $S_{5.8\ \mu\mathrm{m}}/S_{3.6\ \mu\mathrm{m}}$ colour diagram. Equation 2 in [4] presents the color cuts used in defining the region.

Firstly, we classified radio excess sources as RL AGN. From the remaining non-radio excess sources, we applied the X-ray luminosity cut and the MIR colour cut to search for signatures of an AGN. We classified non-radio excess sources that met the X-ray AGN and MIR AGN criteria

Category	Sub-category	Count	Percentage (%)	Class
Radio excess	–	1735	33.2	RL AGN
Non-radio excess	X-ray AGN	245	4.7	RQ AGN
	MIR AGN	217	4.2	RQ AGN
	No AGN signature	3026	55.4	SFGs

Table 2: Number of sources classified as RL AGN, RQ AGN, and SFGs using the classification diagnostics outlined in the text. The 131 (2.5%) sources not presented in this table are bad fits from CIGALE.

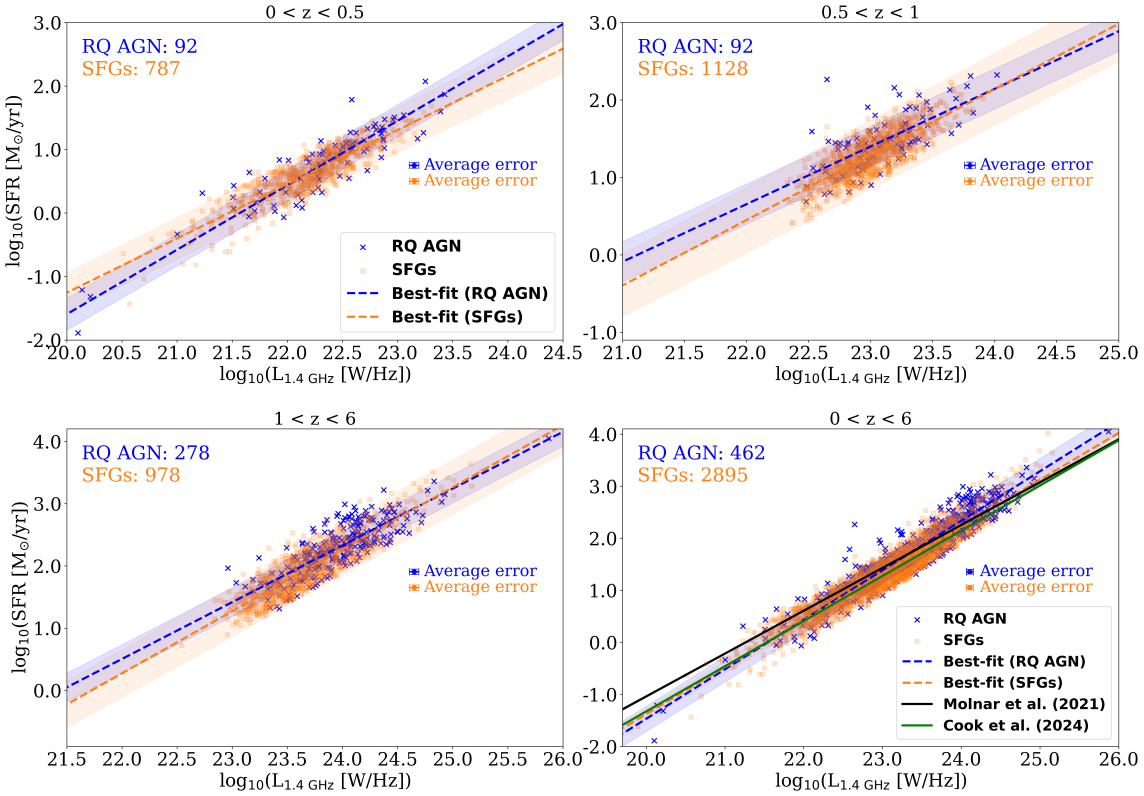

Figure 2: SFRs as a function of $L_{1.4\ \mathrm{GHz}}$ at three redshift bins for the RQ AGN (blue crosses) and the SFGs (orange squares), in the first three plots. The dashed lines represent the best-fit lines for SFGs (orange) and RQ AGN (blue), with the orange and blue shaded areas indicating their 2σ regions of error. The solid lines are the best-fit lines from [7, green] and [8, black]. The last plot shows the relationship between the entire sample of RQ AGN and SFGs.

as RQ AGN. Then, the remaining non-radio excess sources with no signatures of an AGN from the multi-wavelength diagnostics are classified as SFGs. Table 2 presents summarised statistics of these populations.

5. Calibrations of SFR-$L_{1.4\ \mathrm{GHz}}$ relation

In this section, we calibrated the SFR-$L_{1.4\ \mathrm{GHz}}$ correlation for SFGs and RQ AGN at different redshift bins. Table 3 presents the Spearman's correlation coefficients at redshift bins $0 < z < 0.5$, $0.5 < z < 1$, and $1 < z < 6$ for both the SFGs and RQ AGN. The best-fit lines,

Redshift bins	$\log_{10}$(SFR) vs. $\log_{10}(L_{1.4\ \mathrm{GHz}})$		Number of sources per bin	
	RQ AGN	SFGs	RQ AGN	SFGs
$0 < z < 0.5$	0.897 ± 0.007	0.857 ± 0.004	83	817
$0.5 < z < 1$	0.674 ± 0.014	0.748 ± 0.005	140	1120
$1 < z < 6$	0.845 ± 0.005	0.814 ± 0.003	320	1008

Table 3: Spearman rank correlation coefficients (ρ) for the SFR–$L_{1.4\ \mathrm{GHz}}$ relation in different redshift bins for SFGs and RQ AGN. The last column presents the number of sources per redshift bin.

$$\log_{10}\left(\frac{\mathrm{SFR}}{M_\odot/\mathrm{yr}}\right)_{\mathrm{SFGs}} = (0.866 \pm 0.006) \times \log_{10}\left(\frac{L_{1.4\ \mathrm{GHz}}}{\mathrm{W/Hz}}\right) - (18.616 \pm 0.142) \quad (3)$$

$$\log_{10}\left(\frac{\mathrm{SFR}}{M_\odot/\mathrm{yr}}\right)_{\mathrm{RQ\ AGN}} = (0.926 \pm 0.003) \times \log_{10}\left(\frac{L_{1.4\ \mathrm{GHz}}}{\mathrm{W/Hz}}\right) - (19.911 \pm 0.148), \quad (4)$$

were fitted to the entire sample of SFGs and RQ AGN. We obtained the best-fit slopes of $m_{\mathrm{SFGs}} \approx 0.866 \pm 0.006$ with a scatter $\sigma_{\mathrm{SFGs}} \approx$ of 0.22 ± 0.003 dex and $m_{\mathrm{RQ\ AGN}} \approx 0.926 \pm 0.003$ with a scatter of $\sigma_{\mathrm{RQ\ AGN}} \approx 0.28 \pm 0.009$ dex, respectively. The results are consistent with those of [7], where they obtained the slope of $m_{\mathrm{SFGs}} \approx 0.868 \pm 0.005$. [8] obtained a shallower slope ($m_{\mathrm{SFGs}} \approx 0.823 \pm 0.009$) than the one obtained in this work, and the discrepancy could be because they studied 9645 infrared and radio-detected galaxies in the nearby Universe ($z < 0.2$). In contrast, our study goes up to $z \sim 6$. These results indicate that radio continuum emission in RQ AGN from the MIGHTEE Early Science COSMOS field catalogue predominantly traces SF. They also imply that there is less contribution from the AGN jet component.

6. Conclusions

We used 5223 MIGHTEE Early Science images and their multi-wavelength counterparts detected in the COSMOS field. This catalogue of radio-detected sources traced up to $z \approx 6$, was used to study whether radio continuum emission in RQ AGN predominantly traces SF, and the main results are:

- The detected source population is divided into RL AGN (33.2%), RQ AGN (8.9%), and SFGs (55.4%) using the multi-wavelength diagnostics.
- We calibrated the SFR-$L_{1.4\ \mathrm{GHz}}$ relation for SFGs and RQ AGN in redshift bins and obtained the average Spearman's rank coefficient of $\rho_{\mathrm{SFGs}} \approx 0.806 \pm 0.004$ and $\rho_{\mathrm{RQ\ AGN}} \approx 0.805 \pm 0.009$, respectively. We also fitted the best-fit lines to a whole sample of SFGs and RQ AGN and obtained the linear slopes of $m_{\mathrm{SFGs}} \approx 0.866 \pm 0.006$ and $m_{\mathrm{RQ\ AGN}} \approx 0.926 \pm 0.003$, respectively, with the scatters of $\sigma_{\mathrm{SFGs}} \approx 0.220 \pm 0.003$ dex and $\sigma_{\mathrm{RQ\ AGN}} \approx 0.28 \pm 0.009$ dex, consistent with results from the literature. Based on the agreement between the Spearman's coefficients and the slopes for SFGs and RQ AGN, we conclude that radio continuum emission from the MIGHTEE-detected RQ AGN predominantly traces SF.

Acknowledgments

The authors are grateful for financial support from the National Research Foundation (NRF), South Africa, and acknowledge support from the South African Gamma-Ray Astronomy Programme (SA-GAMMA). The MeerKAT telescope is operated by the South African Radio Astronomy Observatory, which is a facility of the National Research Foundation, an agency of the Department of Science and Innovation. We acknowledge the use of the ilifu cloud computing facility - www.ilifu.ac.za, a partnership between the University

of Cape Town, the University of the Western Cape, Stellenbosch University, Sol Plaatje University, the Cape Peninsula University of Technology and the South African Radio Astronomy Observatory. The ilifu facility is supported by contributions from the Inter-University Institute for Data Intensive Astronomy (IDIA - a partnership between the University of Cape Town, the University of Pretoria and the University of the Western Cape), the Computational Biology division at UCT and the Data Intensive Research Initiative of South Africa (DIRISA).

References

[1] Delvecchio, I., Daddi, E., Sargent, M. T., Jarvis, M. J., Elbaz, D., Jin, S., Liu, D., Whittam, I. H., Algera, H., Carraro, R., *et al.* 2021, *A&A*, 647, A123.

[2] Panessa, F., Baldi, R. D., Laor, A., Padovani, P., Behar, E., & McHardy, I. 2019, *Nat. Astron.*, 3, 387–396.

[3] Szokoly, G. P., Bergeron, J., Hasinger, G., Lehmann, I., Kewley, L., Mainieri, V., Nonino, M., Rosati, P., Giacconi, R., Gilli, R., *et al.* 2004, *ApJS*, 155, 271.

[4] Donley, J. L., Koekemoer, A. M., Brusa, M., Capak, P., Cardamone, C. N., Civano, F., Ilbert, O., Impey, C. D., Kartaltepe, J. S., Miyaji, T., *et al.* 2012, *ApJ*, 748, 142.

[5] Heckman, T. M., & Best, P. N. (2014). The coevolution of galaxies and supermassive black holes: insights from surveys of the contemporary universe. *Annual Review of Astronomy and Astrophysics*, 52(1), 589–660.

[6] Whittam, I. H., Prescott, M., Hale, C. L., Jarvis, M. J., Heywood, I., An, F., Glowacki, M., Maddox, N., Marchetti, L., Morabito, L. K., *et al.* 2024, *MNRAS*, 527, 3231–3245.

[7] Cook, R. H. W., Davies, L. J. M., Rhee, J., Hale, C. L., Bellstedt, S., Thorne, J. E., Delvecchio, I., Collier, J. D., Dodson, R., Driver, S. P., *et al.* 2024, *MNRAS*, 531, 708–727.

[8] Molnár, D. Cs., Sargent, M. T., Leslie, S., Magnelli, B., Schinnerer, E., Zamorani, G., Delhaize, J., Smolčić, V., Tisanić, K., & Vardoulaki, E. (2021). *Monthly Notices of the Royal Astronomical Society*, 504(1), 118–145.

[9] Jonas, J., & the MeerKAT Team. 2016, *MeerKAT Science: On the Pathway to the SKA*, 1.

[10] Briggs, D. S. 1995, *Bull. Am. Astron. Soc.*, 27, 1444.

[11] Mohan, N., & Rafferty, D. 2015, *Astrophysics Source Code Library*, ascl–1502.

[12] Tanaka, M., Hasinger, G., Silverman, J. D., Bickerton, S., Furusawa, H., Harikane, Y., Hu, E., Ikeda, H., Li, Y., McCracken, H. J., *et al.* 2017, *arXiv preprint arXiv:1706.00566*.

[13] Cuillandre, J. C. J., Peck, A. B., Seaman, R. L., & Comeron, F. 2012, *Proc. SPIE Conf. Ser.*, 8448.

[14] Furusawa, H., Kashikawa, N., Kobayashi, M. A. R., Dunlop, J. S., Shimasaku, K., Takata, T., Sekiguchi, K., Naito, Y., Furusawa, J., Ouchi, M., *et al.* 2016, *ApJ*, 822, 46.

[15] Poglitsch, A., Waelkens, C., Bauer, O. H., Cepa, J., Feuchtgruber, H., Henning, T., Van Hoof, C., Kerschbaum, F., Krause, O., Renotte, E., *et al.* 2010, *38th COSPAR Scientific Assembly*, 38, 13.

[16] Rieke, G. H., Young, E. T., Engelbracht, C. W., Kelly, D. M., Low, F. J., Haller, E. E., Beeman, J. W., Gordon, K. D., Stansberry, J. A., Misselt, K. A., *et al.* 2004, *ApJS*, 154, 25.

[17] Griffin, M. J., Abergel, A., Abreu, A., Ade, P. A. R., André, P., Augueres, J.-L., Babbedge, T., Bae, Y., Baillie, T., Baluteau, J.-P., *et al.* 2010, *A&A*, 518, L3.

[18] Steinhardt, C. L., Speagle, J. S., Capak, P., Silverman, J. D., Carollo, M., Dunlop, J., Hashimoto, Y., Hsieh, B.-C., Ilbert, O., Le Fèvre, O., *et al.* 2014, *ApJL*, 791, L25.

[19] Yang, G., Boquien, M., Buat, V., Burgarella, D., Ciesla, L., Duras, F., Stalevski, M., Brandt, W. N., & Papovich, C. 2020, *MNRAS*, 491, 740–757.

[20] Burgarella, D., Buat, V., & Iglesias-Páramo, J. 2005, *MNRAS*, 360, 1413–1425.

[21] Boquien, M., Burgarella, D., Roehlly, Y., Buat, V., Ciesla, L., Corre, D., Inoue, A. K., & Salas, H. 2019, *A&A*, 622, A103.

[22] Whittam, I. H., Jarvis, M. J., Hale, C. L., Prescott, M., Morabito, L. K., Heywood, I., Adams, N. J., Afonso, J., An, F., Ao, Y., *et al.* 2022, *MNRAS*, 516, 245–263.

[23] Rivera, G. C., Lusso, E., Hennawi, J. F., & Hogg, D. W. 2016, *ApJ*, 833, 98.

[24] Yun, M. S., Reddy, N. A., & Condon, J. J. 2001, *ApJ*, 554, 803.

[25] Condon, J. J. 1992, *ARA&A*, 30, 575–611.

[26] Drake, A. B., Smith, D. J. B., Hardcastle, M. J., Best, P. N., Kondapally, R., Arnaudova, M. I., Das, S., Shenoy, S., Duncan, K. J., Röttgering, H. J. A., *et al.* 2024, *MNRAS*, 534, 1107–1126.

[27] Das, S., Smith, D. J. B., Haskell, P., Hardcastle, M. J., Best, P. N., Duncan, K. J., Arnaudova, M. I., Shenoy, S., Kondapally, R., Cochrane, R. K., *et al.* 2024, *MNRAS*, 531, 977–996.

[28] Best, P. N., Kondapally, R., Williams, W. L., Cochrane, R. K., Duncan, K. J., Hale, C. L., Haskell, P., Małek, K., McCheyne, I., Smith, D. J. B., *et al.* 2023, *MNRAS*, 523, 1729–1755.

[29] White, S. V., Delvecchio, I., Adams, N., Heywood, I., Whittam, I. H., Hale, C. L., Namane, N., Bowler, R. A. A., & Collier, J. D. 2025, *MNRAS*, staf1187.

[30] White, S. V., Jarvis, M. J., Häußler, B., & Maddox, N. 2015, *MNRAS*, 448, 2665–2686.

[31] White, S. V., Jarvis, M. J., Kalfountzou, E., Hardcastle, M. J., Verma, A., Cao Orjales, J. M., & Stevens, J. 2017, *MNRAS*, 468, 217–238.

[32] Bonzini, M., Mainieri, V., Padovani, P., Andreani, P., Berta, S., Bethermin, M., Lutz, D., Rodighiero, G., Rosario, D., Tozzi, P., *et al.* 2015, *MNRAS*, 453, 1079–1094.

[33] Morabito, L. K., Sweijen, F., Radcliffe, J. F., Best, P. N., Kondapally, R., Bondi, M., Bonato, M., Duncan, K. J., Prandoni, I., Shimwell, T. W., *et al.* 2022, *MNRAS*, 515, 5758–5774.

[34] Jarvis, M., Taylor, R., Agudo, I., *et al.* 2016, *preprint*, 6.

[35] Carilli, C., & Rawlings, S. 2004, *arXiv preprint astro-ph/0409274*.

[36] Wilson, T. L., Rohlfs, K., & Hüttemeister, S. 2009, *Tools of Radio Astronomy*, Springer.

[37] Chabrier, G. 2003, PASP, 115, 763

[38] Bruzual, G., & Charlot, S. 2003, MNRAS, 344, 1000

[39] Calzetti, D., Armus, L., Bohlin, R. C., et al. 2000, ApJ, 533, 682

[40] Dale, D. A., Helou, G., Magdis, G. E., et al. 2014, ApJ, 784, 83